ACS APPLIED MATERIALS & INTERFACES

Open Access

This article is licensed under CC-BY 4.0

www.acsami.org

Research Article

Nanostructure-Enabled Apparent Slip through Dynamic Hydration Reorganization

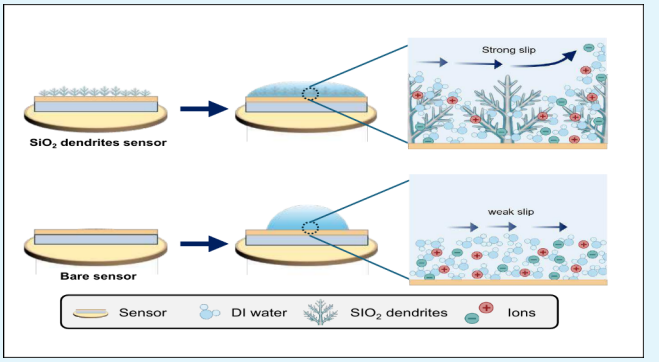
Youngho Han,‖ Aoife Lundberg,‖ Jong Sik Kim, Paul Cannon, Doojin Lee,* Enda McGlynn,* and Nikhil Bhalla*

Cite This: *ACS Appl. Mater. Interfaces* 2026, 18, 60124−60136

Read Online

ACCESS | Metrics & More | Article Recommendations | Supporting Information

ABSTRACT: Dynamic transport across solid–liquid nanointerfaces is commonly interpreted through equilibrium wettability, although increasing evidence suggests that interfacial hydration rather than contact angle governs nanoscale liquid motion. However, how hydration reorganizes under ionic and hydrodynamic perturbations at strongly hydrophilic nanostructured interfaces remains poorly understood. Here, we demonstrate that dendritic silica nanostructures create a hydration-rich interphase whose dynamic mechanical state can be programmed by electrolyte concentration, flow, and biomolecular adsorption. Contact-angle measurements, density functional theory calculations, and overtone-resolved quartz crystal microbalance with dissipation monitoring reveal that intermediate ionic strengths maximize near-surface acoustic loading without a proportional increase in dissipation, while increasing flow induces a flow-dependent enhancement in model-derived apparent mobility. The response is strongest at higher overtones and persists after bovine serum albumin adsorption, demonstrating that the adaptive hydration state survives the formation of a complex protein–water interphase. Rather than reflecting the classical hydrophobic slip, the observations identify a dynamically reconfigurable hydration layer that decouples equilibrium wettability from interfacial mechanics. These findings establish hydration-layer reconfigurability as a general mechanism governing liquid mobility at hydrophilic nanostructured interfaces and provide a design framework for nanofluidic transport, antifouling materials, separation membranes, and interfacial biosensing technologies.



KEYWORDS: *QCM-D, apparent slip, hydration-layer reorganization, dendritic SiO_2 nanostructures, solid–liquid interface*

INTRODUCTION

Liquid transport at solid–liquid nanointerfaces governs processes ranging from nanofluidic separations and membrane transport to lubrication, electrokinetics, and surface-based biosensing. At the continuum scale, the interfacial boundary is commonly represented by the Navier slip condition, with the slip length describing the degree of solid–liquid momentum transfer. Early velocimetric, force-based, and fluctuation-based measurements established that smooth hydrophilic glass and silica generally approach a no-slip condition, whereas smooth nonwetting surfaces may exhibit modest slip.[1−4] Molecular simulations similarly predict that increasing solid–liquid surface attraction suppresses slip by increasing interfacial friction and slowing the relaxation of interfacial water.[5] However, recent nanoscale mapping has shown that contact angle does not uniquely determine slip and that topographical steps, chemical heterogeneity, nanobubbles, and adsorbed ions can strongly bias the apparent response.[6] Wettability is therefore an incomplete descriptor of the dynamic mechanical state of an aqueous nanointerface.

Surface structure further complicates this relationship. Experiments on nanopatterning can amplify either hydrophilicity or hydrophobicity by altering liquid penetration and the fraction of solid–liquid contact,[7] while gas-retaining superhydrophobic structures can generate large effective slip through a composite solid–liquid–air boundary as measured experimentally.[8] Exceptional water transport has also been measured experimentally in carbon nanotube membranes and individual nanotubes, where atomically smooth graphitic walls support radius-dependent interfacial slippage.[9,10] Molecular dynamics simulations have further shown that even nominally hydrophobic nanochannels can undergo a slippery-to-sticky

Received: August 12, 2026
Revised: October 1, 2026
Accepted: October 5, 2026
Published: October 22, 2026



Downloaded from pubs.acs.org/aamick/article-pdf/18/43/60124/6895925/am-2026-166644.pdf by DUBLIN CITY UNIV user on 05 November 2026

© 2026 The Author(s). Published by American Chemical Society

https://doi.org/10.1021/acsami.6c16664
ACS Appl. Mater. Interfaces 2026, 18, 60124−60136

transition when ions modify the molecular organization and friction of confined water.[11] These observations show that nanoscale flow is governed by a coupled response of surface chemistry, morphology, confinement, ionic structure, and interfacial water rather than by macroscopic contact angle alone. A major unresolved question is whether a strongly hydrophilic, gas-free nanostructure can support an enhanced dynamic mobility through reorganization of its hydration layer.

Hydration provides a plausible route to such behaviour. Water adjacent to polar and charged surfaces forms molecularly layered structures that generate short-range hydration forces, as measured experimentally.[12] Despite strong normal binding, compressed hydration layers have been shown experimentally to retain substantial lateral fluidity through rapid molecular exchange.[13] Simulations of water confined between hydrophilic monolayers likewise show persistent liquid-like diffusion, although its magnitude depends strongly on film thickness and pressure.[14] Hydration lubrication consequently permits surfaces to sustain high normal loads while maintaining low shear resistance.[15] On silica, hydrated cation adsorption has been experimentally shown to reduce lateral friction,[16] but the dissipation pathway was found experimentally to depend on ion size, hydration-shell structure, and sliding rate.[17] Molecular simulations further predict transitions among bulk-viscous, interfacial, and slip-dominated friction as the hydration layer becomes progressively confined,[18] while experiments with multivalent electrolytes show that changes in hydration-layer coverage and structure select distinct lubrication states.[19] Strong surface hydration and enhanced lateral mobility are therefore not mutually exclusive; the missing quantity is the dynamic mechanical reconfigurability of the hydrated interphase.

Quartz crystal microbalance with dissipation monitoring (QCM-D) offers a sensitive route to this dynamic interphase because it measures the complex acoustic load generated by an oscillating solid in contact with a liquid. The classical liquid-loading relation connects the resonance shift to liquid density and viscosity,[20] while dissipation monitoring enables simultaneous measurement of energy loss during each oscillation cycle.[21] Viscoelastic load models further relate overtone-dependent frequency and dissipation responses to the mechanical properties of interfacial films.[22] Interpretation is nevertheless nontrivial: nanoroughness increases the quantity of mechanically trapped water,[23] and the acoustic mass of biomolecular layers has been measured to substantially exceed their nonsolvated mass because QCM-D senses coupled solvent.[24,25] Heterogeneous layers are predicted theoretically to produce overtone-dependent responses through local hydrodynamic and viscoelastic coupling.[26] Recent load-impedance theories and particle-deposition studies demonstrate that reactive frequency loading and dissipative loss cannot generally be reduced to gravimetric mass and may vary strongly with hydrodynamic penetration depth, particle coverage, and interfacial structure.[27−29] Accordingly, QCM-D does not directly measure a liquid velocity profile or a Navier slip length, but it can reveal reproducible deviations from a selected no-slip acoustic boundary model.

Here, we test the hypothesis that a strongly hydrophilic nanostructure can create a flow-reconfigurable hydration interphase whose dynamic boundary condition is not predictable from static wettability. Dendritic SiO_2 is formed on a gold-coated quartz sensor to generate a high-surface area, silanol-rich interface containing both molecularly associated and geometrically confined water. Scanning electron microscopy and contact-angle measurements establish the morphology and equilibrium wetting state, while density functional theory calculations evaluate water binding at representative silica sites. Overtone-resolved QCM-D measurements then probe how electrolyte concentration and flow reorganize the complex acoustic load, and a vibrating-interface model is used to extract a dimensionless apparent-mobility parameter relative to a no-slip reference. Bovine serum albumin adsorption provides a biomolecular test because protein-associated acoustic layers incorporate both viscoelastic matter and substantial interfacial water.[30]

We show that ionic strength and hydrodynamic forcing jointly program the hydrated acoustic boundary. Intermediate electrolyte conditions produce a nonmonotonic near-surface response, while increasing flow enhances reactive loading and model-derived apparent mobility without a proportional rise in dissipation. The effect is strongest at higher overtones and persists after protein adsorption, indicating that the dendritic interface supports an adaptive protein–solid–liquid interphase rather than a fixed wetting-defined boundary. These results distinguish equilibrium wettability from dynamic interfacial mechanics and identify hydration-layer reconfigurability as a design principle for controlling apparent liquid mobility at strongly hydrophilic nanointerfaces.[31−33]

■ EXPERIMENT

Materials

Piezoelectric quartz crystals with a resonant frequency of 10 MHz were purchased from Open QCM, Italy (AT10-14-12-AU-WRAP). Phosphate-buffered saline (PBS) (P4417, Sigma-Aldrich, United Kingdom) was used to prepare various concentrations of water-based ionic solution. Dissolving one tablet in 200 mL of deionized water yields concentrations of 10 mM phosphate buffer, 2.7 mM potassium chloride, and 137 mM sodium chloride (pH 7.4 at 25 °C). This 10 mM PBS solution was serially diluted tenfold with deionized water to obtain PBS solutions ranging from 1 nM to 1 mM, namely 1 nM, 10 nM, 100 nM, 1 μM, 10 μM, 100 μM, and 1 mM (Table S1).

SiO_2 Coating on the Quartz Crystal Surfaces

The sensing elements used in this work were quartz crystals bearing a SiO_2 overlayer deposited by a PVD route based on the thermal decomposition of polydimethylsiloxane (PDMS) (Sylgard 184 silicone elastomer kit, Dow, USA) in air, together with bare gold-coated quartz crystals. Prior to coating, the crystals were sonicated in acetone for 10 min, then rinsed with acetone, and this sequence was repeated using isopropyl alcohol (IPA). Samples were then gently dried under a stream of dry nitrogen. A mass of 70 mg of PDMS was placed at one end of an alumina crucible, with the substrates positioned at the opposite end, 5.5 cm away from the block of PDMS, lying across the boat, supported by a 2 cm × 1.5 cm Si coupon. This alumina boat was positioned inside a hollow quartz tube (3.8 cm inner diameter), and the quartz tube was placed in the center of a muffle furnace (Muffle Furnace LT 3/11/B410, Nabertherm, Germany), with the samples to be coated located between the PDMS block and the furnace exhaust. The furnace was heated to 500 °C using a ramp rate of 40 °C/min, and this temperature was maintained for two hours. The furnace was allowed to cool to room temperature before removing the samples.[34,35]

QCM Measurements

All measurements were performed on a QCM-D (openQCM NEXT, Open QCM, Italy), equipped with dissipation monitoring,

Downloaded from pubs.acs.org/aamick/article-pdf/18/43/60124/6895925/am-2026-166644.pdf by DUBLIN CITY UNIV user on 05 November 2026

https://doi.org/10.1021/acsami.6c16664
ACS Appl. Mater. Interfaces 2026, 18, 60124−60136

simultaneous multiple overtones measurement, and active thermal control capabilities. The temperature was held constant at 25 °C throughout, and the drive voltage was set to 400 mV, corresponding to a mechanical vibration amplitude of approximately 3–3.5 nm. Before each measurement, the quartz crystal was cleaned with deionized water and IPA. For all measurements, the sensor was stabilized for 100 s, and the stable signal in air was used as the reference for calculating Δf and ΔD. Two types of measuring configurations were employed. In the drop configuration, the quartz crystal was mounted in the pipetting module, and 200 μL of either deionized water or PBS solution of the relevant concentration was pipetted directly onto the exposed crystal surface. For the flow configuration, the quartz crystal was mounted in the optical module, and either deionized water or PBS solution of the relevant concentration was delivered across the crystal surface using a syringe pump (Fusion 200-X, Chemyx, USA). Due to the non-parallel alignment of the optical module's inlet with the crystal surface, the injected flow could impose an extra force on the oscillating crystal, influencing the QCM response. The flow rates were increased stepwise from 1 to 32 mL/h (1, 2, 4, 8, 16, and 32 mL/h). Δf and ΔD were calculated as the difference between air reference and the stable signals obtained during measurement. All measurements were repeated three times. The measurements using only PBS solution were performed on a single crystal, whereas measurements with BSA were performed on a separate crystal. Error bars represent standard error of the mean in all figures.

Scanning Electron Microscopy Analysis

The morphology of the samples was characterized by scanning electron microscopy (SEM) (JSM-IT100, Jeol, Japan) in secondary electron emission mode. Images were acquired at an accelerating voltage of 5 kV and magnifications ranging from 4500 to 6500×, and were used to assess the uniformity of SiO_2 dendrite growth across the sample surface.

Contact Angle Measurements

Wetting behavior was evaluated by contact angle measurements (OCA35, DataPhysics Instruments, Germany) using a droplet volume of ∼5 μL. Contact angles were measured on both bare gold-coated quartz crystals and SiO_2 dendrites-coated quartz crystals. All samples were cleaned with acetone and IPA prior to contact angle measurements. A deionized water droplet was deposited on each crystal, and the measurement was repeated three times.

Density Functional Theory Calculations

To rationalize the wetting behavior observed experimentally, density functional theory (DFT) calculations were performed using the r^{2}SCAN-3c composite method implemented in ORCA to examine the interaction between water and the SiO_2 nanostructured surface. The surface was represented by models terminating in the two representative surface groups of silica, silanol (Si–OH) and siloxane (Si–O–Si), with the siloxane case subdivided into two approach orientations, giving three adsorption configurations in total (Models 1–3). Since the models contained only H, O, and Si, all calculations were all-electron and no pseudopotentials (effective core potentials) were used. Non-bonded interactions were accounted for by the D4 dispersion correction, and basis set superposition error by the geometrical counterpoise (gCP) correction, both of which are included in the r^{2}SCAN-3c scheme. TightSCF was applied to impose stricter convergence criteria for self-consistent field calculations, and TightOpt was used for geometry optimization so that the structures were converged with respect to energy, gradient, and atomic displacement. A more negative value indicates stronger adsorption. For comparison, E_{ads} values were normalized to that of Model 1.

RESULTS AND DISCUSSION

Formation of a Hydration-Rich Dendritic Silica Interface

Dendritic SiO_2 nanostructures were formed on the gold-coated quartz sensor to create a high-surface area, hydroxyl-rich solid–liquid interface capable of supporting a strongly hydrated boundary layer. The conceptual architecture in Figure 1a distinguishes this interface from a conventional smooth hydrophilic surface. Water molecules and solvated ions can occupy the interstitial volume between the dendritic features, whereas silanol and siloxane surface sites provide multiple interaction sites for interfacial water. Consequently, the liquid mechanically sensed by the oscillating quartz comprises not only the bulk solution but also surface-associated water, ion-associated hydration shells, and liquid confined within the nanostructured layer. The scanning electron microscopy images in Figure 1b,c confirm the formation of a dense and spatially distributed dendritic morphology over the sensor surface. Further images at higher and lower magnification are shown in Figure S1. The branched structures substantially increase the geometric surface area and nanoscale roughness relative to the underlying gold electrode. This morphology is important because the QCM-D response of a rough or porous interface includes contributions from liquid hydrodynamically coupled within surface asperities and interstitial voids. The resulting acoustic load therefore cannot be interpreted as a simple dry surface mass. Previous studies have shown that the quantity of solvent mechanically sensed by QCM-D increases with nanoscale surface roughness and that the acoustic mass of an adsorbed interfacial layer can include a substantial contribution from coupled water.[23,24]

Surface wetting changed significantly following the formation of the SiO_2 dendrites. The static water contact angle decreased from approximately 61.1° on the bare surface to 14.1° on the dendritic surface (Figure 1d–f), confirming the formation of a strongly hydrophilic interface. XPS analysis showed a low carbon content on the SiO_2-coated surface (Figure S9), and the droplet spread similarly with and without UV treatment (Movies S1 and S2), indicating that residual carbon has a negligible effect on the wettability. Both the nanoscale roughness and surface chemistry of the dendritic SiO_2 may contribute to this decrease. However, their individual contributions cannot be quantitatively separated because the contribution due to the roughness of the randomly grown dendritic structures cannot be precisely defined. In addition, the contact angle is a static macroscopic measurement and does not reveal the molecular organization of interfacial water. DFT calculations were therefore used to evaluate water adsorption at representative silica surface sites. The representative sites are silanol (Si–OH) site and two siloxane (Si–O–Si) sites differing in the approach of water toward either the bridging oxygen or the silicon atom, giving three adsorption configurations in total (Figure 1g,h). The adsorption energy was defined as

$$E_{ads} = E_{surface+H_2O} - E_{surface} - E_{H_2O} \quad (1)$$

where $E_{surface+H_2O}$ is the total energy of the hydrated surface model, $E_{surface}$ is the energy of the isolated surface, and E_{H_2O} is the energy of an isolated water molecule. A more negative value of E_{ads} corresponds to more energetically favourable water adsorption. The calculated adsorption energies show favourable interaction between water and all of the modelled

Downloaded from pubs.acs.org/aamick/article-pdf/18/43/60124/6895925/am-2026-16664d.pdf by DUBLIN CITY UNIV user on 05 November 2026

https://doi.org/10.1021/acsami.6c16664
ACS Appl. Mater. Interfaces 2026, 18, 60124–60136

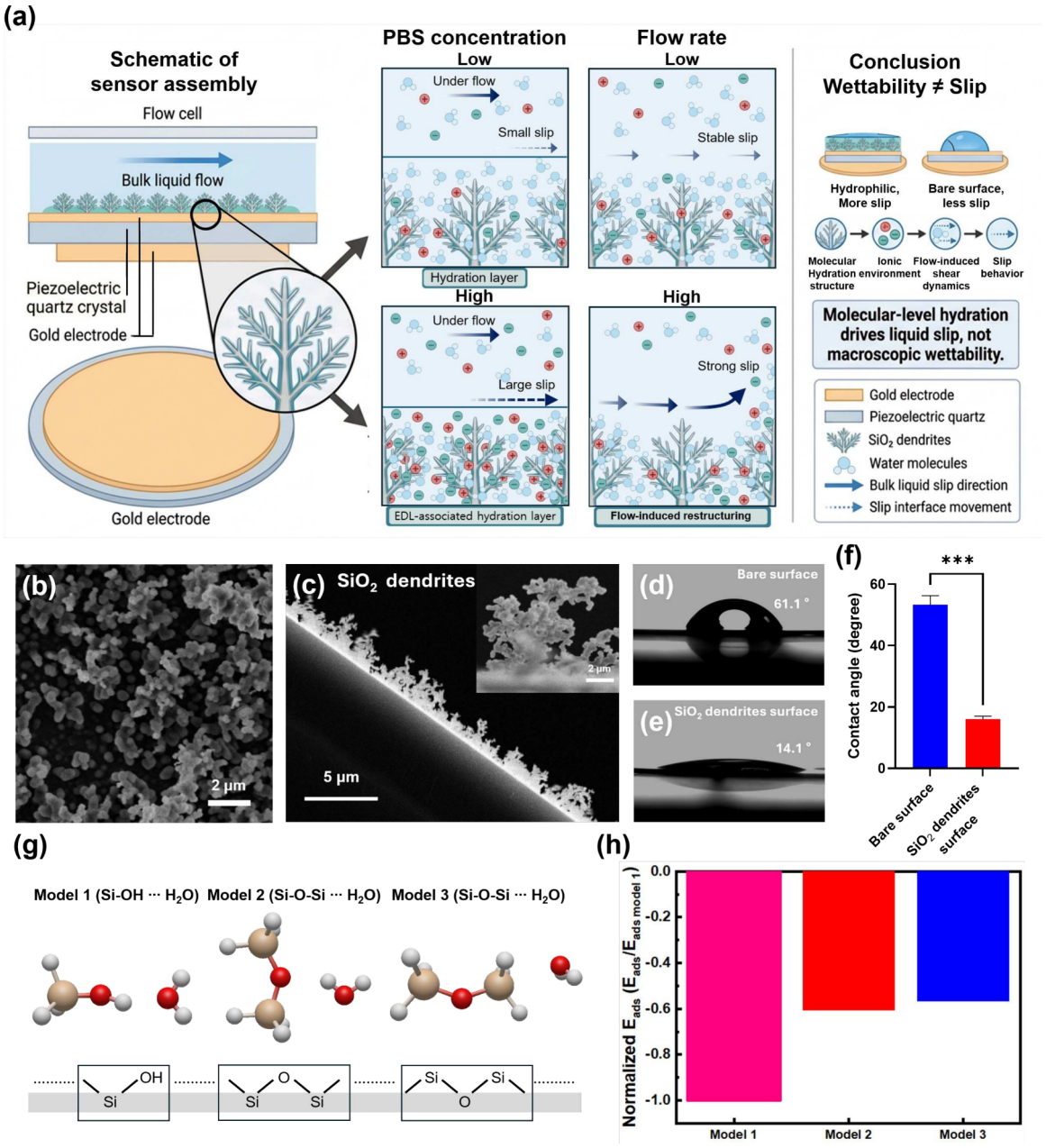


Figure 1. Hydration-mediated apparent slip at dendritic SiO_2 interfaces. (a) Schematic of the QCM-based sensor assembly and the proposed effects of PBS concentration and flow rate on hydration-layer formation, EDL formation, and flow-induced reorganization. (b,c) SEM images confirming the formation of dendritic SiO_2 nanostructures on the sensor surface. (d,e) Representative water-contact-angle images of the bare and dendritic surfaces. (f) Quantitative contact-angle comparison demonstrates the substantial increase in surface hydrophilicity after dendrite formation. Error bars represent the standard error of three independent measurements for each surface (g) Density functional theory models of water adsorption at representative Si–OH and two siloxane (Si–O–Si) sites differing in the approach of water toward either the bridging oxygen or the silicon atom. (h) Normalized DFT adsorption energies showing favourable water interaction with the hydroxyl-rich SiO_2 interface.

silica sites, with the strongest interaction associated with hydroxyl-mediated adsorption. ($E_{ads} \approx -26$ kJ/mol for Si–OH, compared with ≈–15.7 and –14.6 kJ/mol for the two Si–O–Si configurations; Table S2). This result indicates that surface silanol groups stabilize water through hydrogen bonding and may promote the formation of a hydration layer. However, these cluster models do not fully represent the structural and chemical heterogeneity of the experimental surface. The calculations were used only to compare the relative affinity of water for representative surface groups and are therefore interpreted qualitatively. The DFT results show favorable water adsorption at the model silica sites, which is consistent with, but does not directly confirm, the hydration state of the experimental interface. Together with the contact-angle measurements, these results support the formation of a strongly hydrophilic, hydration-rich interface rather than a surface modified only by increased roughness. This distinction is central to the interpretation of the subsequent

https://doi.org/10.1021/acsami.6c16664
ACS Appl. Mater. Interfaces 2026, 18, 60124–60136

Downloaded from pubs.acs.org/aamick/article-pdf/18/43/60124/6895925/am-2026-166644.pdf by DUBLIN CITY UNIV user on 05 November 2026

measurements. A low contact angle is conventionally associated with strong solid–liquid adhesion and a no-slip hydrodynamic boundary. The present system instead tests whether a strongly hydrated interface can remain structurally associated with the solid while permitting dynamic reorganization within the liquid-facing region of the interphase. Hydration-lubrication studies have demonstrated that water associated with charged or polar groups can resist normal compression while retaining rapid molecular exchange and lateral mobility under shear. Similar behaviour has been reported for hydrated ions confined between charged surfaces and for cation-mediated lubrication of silica interfaces.[15,16] The present QCM-D measurements do not directly measure friction, and the hydration-lubrication analogy should therefore not be regarded as direct evidence of a tribological lubrication mechanism. Nevertheless, it provides a physically plausible framework for a boundary layer that is strongly hydrated while remaining dynamically compliant.

Ionic Strength Programs the Overtone-Resolved Acoustic Boundary State

The baseline acoustic response of the dendritic SiO_2 interface was first evaluated in deionized water and PBS solutions spanning 1 nM to 1 mM (Figure 2). The frequency and dissipation data show that electrolyte addition does not produce a uniform shift across the overtone series. Instead, the response becomes progressively more sensitive to the ionic environment at the higher overtones, indicating that the interfacial liquid cannot be treated as a homogeneous extension of the bulk phase. At the fundamental mode, $n1$, the magnitude of the frequency shift remains narrowly distributed between approximately 4.59 and 4.63 kHz (Figure 2a). This weak concentration dependence indicates that the overall coupled liquid load sampled by the fundamental mode is broadly conserved across the tested electrolyte range. By contrast, $n3$ and $n5$ exhibit clearer and nonmonotonic ionic-strength dependences. At $n3$, $|\Delta f|$ increases from approximately 9.12 kHz in deionized water to approximately 9.24 to 9.27 kHz at intermediate PBS concentrations (Figure 2b). At $n5$, the response increases from approximately 11.53 kHz in deionized water to a maximum of approximately 11.85 to 11.90 kHz between 10 and 100 μM PBS, followed by a reduction at 1 mM (Figure 2c). In contrast, the bare gold-coated crystal showed smaller shifts without systematic concentration dependence (Figure S7).

The nonmonotonic response is mechanistically more informative than a simple proportional increase with electrolyte concentration. Increasing PBS concentration simultaneously changes ion availability, electrostatic screening of the electric double layer (EDL), ion–surface association, hydration-shell population, and the organization of water within the dendritic volume. At low ionic strength, the silica surface is strongly hydrated but contains relatively few associated counterions. At intermediate ionic strength, hydrated ions may increase the mechanically coupled interfacial volume and reorganize the hydrogen-bonding network surrounding the silanol-rich surface. At higher ionic strength, stronger electrostatic screening and compression of the interfacial ionic environment may reduce the spatial extent or mechanical compliance of this region. The maximum response observed at intermediate PBS concentration is therefore consistent with an optimum in ion-assisted hydration coupling rather than with a direct proportionality between electrolyte concentration and effective acoustic

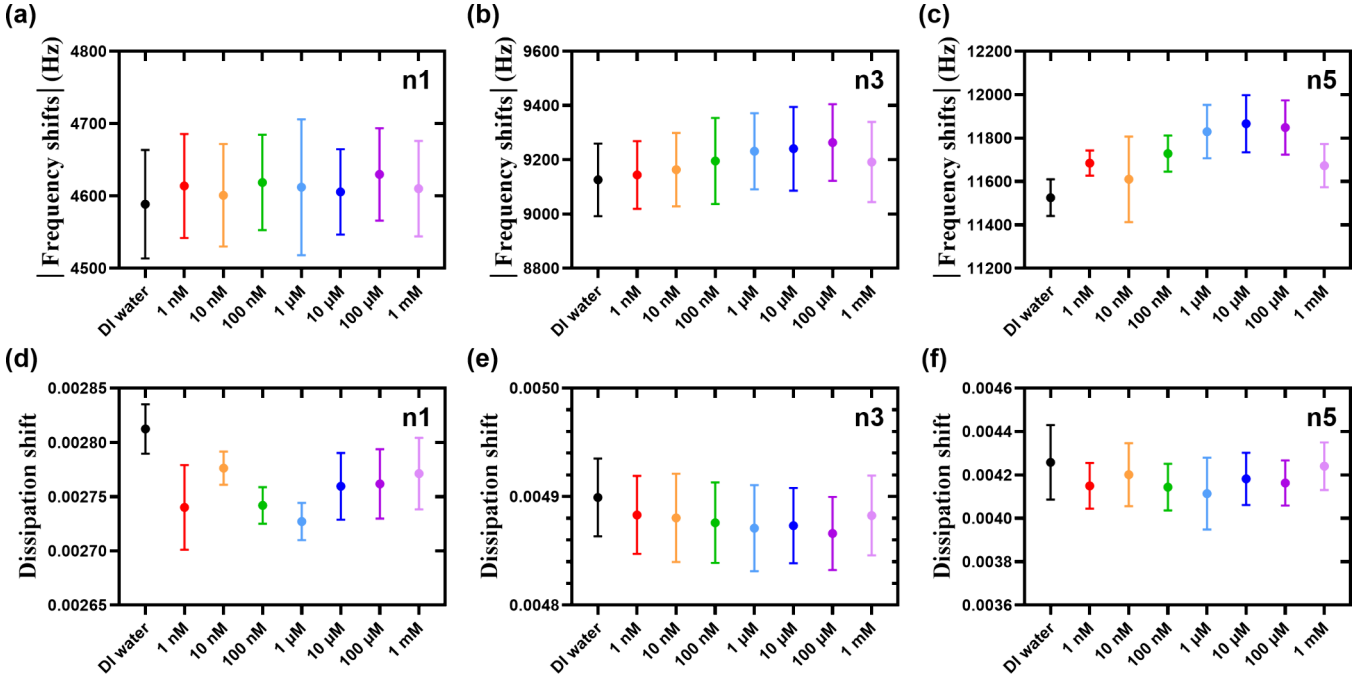


Figure 2. Overtone-resolved QCM-D response of the strongly hydrophilic nanostructured solid–liquid interface under different hydration and ionic conditions. (a–c) Absolute frequency shifts, $|\Delta f|$, measured at $n1$, $n3$, and $n5$, respectively, in deionized water and PBS solutions ranging from 1 nM to 1 mM. The higher overtones exhibit a more pronounced electrolyte dependence than the fundamental mode. (d–f) Corresponding dissipation shifts. Dissipation remains comparatively stable or decreases slightly following PBS addition, indicating that ionic hydration reorganizes the interfacial layer without producing a proportional increase in viscous energy loss.

Downloaded from pubs.acs.org/aamick/article-pdf/18/43/60124/6895925/am-2026-166644.pdf by DUBLIN CITY UNIV user on 05 November 2026

https://doi.org/10.1021/acsami.6c16664
ACS Appl. Mater. Interfaces 2026, 18, 60124–60136

loading. The overtone dependence further supports this interpretation. For a Newtonian liquid, the acoustic shear-wave penetration depth is

$$\delta_n = \left(\frac{2\eta}{\rho\omega_n}\right)^{1/2} \quad (2)$$

where η is the liquid viscosity, ρ is the liquid density, and ω_n is the angular oscillation frequency at overtone n. Because δ_n decreases as the oscillation frequency increases, higher overtones weight a progressively thinner region adjacent to the oscillating surface. The greater electrolyte sensitivity of $n3$ and $n5$ therefore indicates that ionic strength primarily modifies the near-surface EDL-associated hydrated interphase rather than the complete bulk-liquid volume. This interpretation is consistent with load-impedance descriptions of QCM-D measurements, in which frequency shifts in liquid arise from hydrodynamic and viscoelastic coupling and cannot be reduced to gravimetric mass alone.[26−28] In addition, the measured frequency shifts were larger than those predicted by the Kanazawa–Gordon relation, suggesting an interfacial contribution beyond bulk viscous loading. This excess loading may originate from the mechanically coupled EDL and associated hydration.[36] The corresponding dissipation response provides an important complementary constraint. At $n1$, ΔD decreases from approximately 2.81×10^{-3} in deionized water to approximately $2.73–2.78 \times 10^{-3}$ in PBS, with the lowest values occurring at intermediate ionic strengths (Figure 2d). At $n3$, ΔD remains within approximately $4.87–4.90 \times 10^{-3}$, whereas at $n5$ it remains between approximately 4.12×10^{-3} and 4.26×10^{-3} (Figure 2e,f).

Thus, the increase in the higher-overtone frequency response is not accompanied by a proportional increase in dissipative energy loss. If the electrolyte response were governed only by an increase in bulk viscous loading, the reactive and dissipative components of the acoustic load would be expected to change in a more closely coupled manner. Instead, the observed increase in $|\Delta f|$, together with unchanged or slightly reduced ΔD, indicates that electrolyte addition changes the organization and mechanical impedance of the interfacial hydration layer. The resulting interface is therefore best described as a hydration-sensitive mechanical boundary whose balance between coupled liquid inertia and viscous energy loss is regulated by ionic strength. It is important that the raw frequency shifts measured at different overtones are not compared as direct mass measurements. The absolute magnitude of $|\Delta f|$ naturally depends on the oscillation frequency and acoustic-liquid loading. The important result is the increased concentration-dependent deviation at the higher overtones and its decoupling from the dissipation response.

Hydrodynamic Forcing Reorganizes the Hydrated Boundary Layer

The response of the hydrated interface to externally imposed flow was examined by increasing the liquid flow rate from 1 to 32 mL h^{-1} while monitoring the $n1$, $n3$, and $n5$ modes (Figure 3). Across all solution conditions, the magnitude of the frequency shift increases with flow rate, demonstrating that the acoustic boundary state is dynamically responsive to hydrodynamic forcing. At $n1$, $|\Delta f|$ increases from approximately 4.58 to 4.63 kHz at 1 mL h^{-1} to approximately 4.70 to 4.77 kHz at 32 mL h^{-1}, depending on the electrolyte condition (Figure 3a). The flow-induced response becomes progressively

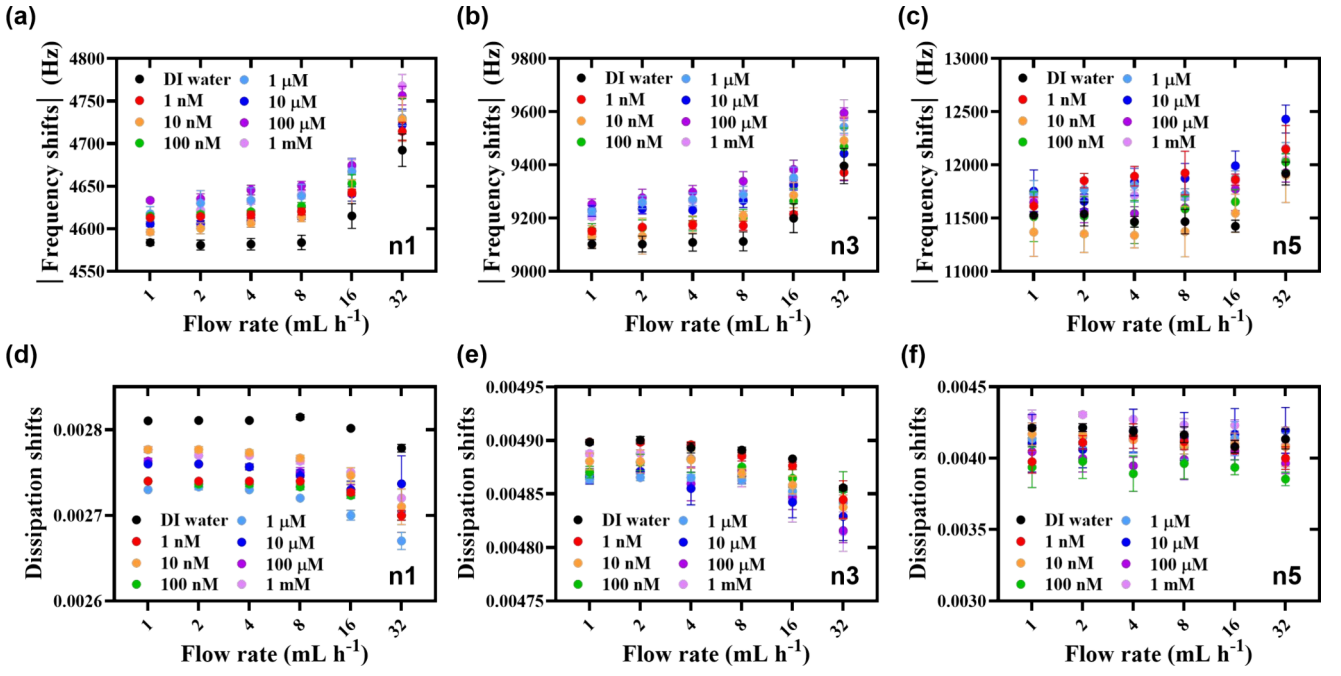


Figure 3. Flow-dependent QCM-D response of the strongly hydrophilic nanostructured solid–liquid interface under different hydration and ionic conditions. (a–c) Absolute frequency shifts, $|\Delta f|$, measured at $n1$, $n3$, and $n5$ as the flow rate is increased from 1 to 32 mL h^{-1}. The flow-induced response becomes progressively stronger at the higher overtones. (d–f) Corresponding dissipation shifts, which remain comparatively stable or decrease slightly with increasing flow. The combination of increasing frequency loading and weakly varying dissipation supports flow-induced reorganization of the hydrated interfacial region.

Downloaded from pubs.acs.org/aamick/article-pdf/18/43/60124/6895925/am-2026-166644.pdf by DUBLIN CITY UNIV user on 05 November 2026

https://doi.org/10.1021/acsami.6c16664
ACS Appl. Mater. Interfaces 2026, 18, 60124−60136

larger at the higher overtones. At $n3$, $|\Delta f|$ increases from approximately 9.12 to 9.25 kHz at low flow to approximately 9.38 to 9.60 kHz at 32 mL h^{-1} (Figure 3b). At $n5$, the response increases from approximately 11.4 to 11.8 kHz to values approaching 12.0 to 12.5 kHz over the same flow interval (Figure 3c). The stronger flow dependence at $n3$ and $n5$ indicates that hydrodynamic forcing predominantly modifies the liquid region nearest to the dendritic surface. A purely bulk-flow effect would be expected to influence the overtone series more uniformly after accounting for the frequency-dependent liquid response. The observed overtone hierarchy is instead consistent with flow-induced rearrangement of confined and surface-associated water within the acoustic penetration depth.

The dissipation response changes considerably less than the frequency response. At $n1$, the deionized-water condition remains close to 2.8×10^{-3} across the flow range, whereas the PBS-containing solutions generally decrease from approximately 2.75–2.78 $\times 10^{-3}$ at low flow to approximately 2.67–2.73 $\times 10^{-3}$ at 32 mL h^{-1} (Figure 3d). At $n3$, ΔD remains within approximately 4.84–4.90 $\times 10^{-3}$ and shows only a modest decrease at the largest flow rates (Figure 3e). Similarly, the $n5$ response remains broadly confined to approximately 3.9–4.3 $\times 10^{-3}$ despite the substantially larger changes in frequency (Figure 3f). In addition, Δf and ΔD are replotted as a function of electrolyte concentration for each flow rate (Figure S2). The bare gold-coated crystal showed a smaller flow-induced increase in $|\Delta f|$ and nearly constant ΔD (Figure S8). This indicates that part of the flow-dependent response arises from generic flow-cell effects, such as the force of the injected flow. The combination of increasing $|\Delta f|$ and nearly invariant or decreasing ΔD is not consistent with a simple mechanism in which increased flow merely adds viscous drag to an unchanged solid–liquid interface. Instead, flow appears to modify how the nanoconfined liquid moves relative to the oscillating surface.

One possible interpretation is that low flow maintains a comparatively disordered or strongly coupled hydration network, whereas increasing flow promotes alignment, molecular exchange, or redistribution of surface-associated water and hydrated ions. The boundary remains acoustically loaded, but the energy dissipated per unit frequency response does not increase proportionally. Such behaviour is consistent with the general concept of a dynamically evolving solid–liquid acoustic interface, in which the QCM-D response contains contributions from both the molecular state of the interphase and its hydrodynamic coupling to the oscillating substrate. Hydrodynamically coupled solvent can substantially influence the complex load impedance, particularly for rough, porous, heterogeneous, or particle-containing interfaces.[26–28] Increasing flow rate can also alter flow-cell pressure, pump pulsation, temperature, and mechanical stress. A flow-dependent frequency shift alone should therefore not be regarded as direct evidence of liquid slip. The mechanistic assignment becomes stronger only when the frequency trend is considered together with the weak dissipation dependence, systematic overtone hierarchy, electrolyte modulation, and model-derived interfacial impedance presented below.

Frequency–Dissipation Decoupling Reveals a Distinct Mechanical Interphase

To examine the relationship between reactive acoustic loading and dissipative energy loss under flow, the coupling between ΔD and $|\Delta f|$ was quantified for each concentration and overtone (Figure 4a–c). For each measurement, ΔD was plotted against $|\Delta f|$ for the flow rates, and the slope $(d(\Delta D)/d(|\Delta f|))$ was obtained by linear regression (Figures S3–S5). The values of Figure 4a–c are the average of the slopes from three independent measurements. These values describe the relationship ΔD and $|\Delta f|$ in response to flow. It is not an intrinsic viscosity or elastic modulus, but it provides a useful means of identifying conditions under which frequency and dissipation cease to scale proportionally.

At $n1$, the slope remains negative, with values of approximately -3.5×10^{-7} to -6.2×10^{-7} Hz^{-1} (Figure 4a). The largest absolute values occur at intermediate ionic strengths, particularly between approximately 10nM and 1μM PBS. At $n3$, the magnitude decreases to approximately -0.6×10^{-7} to -2.2×10^{-7} Hz^{-1} (Figure 4b). At $n5$, the slope approaches zero and becomes weakly positive under selected intermediate PBS conditions. Given that $|\Delta f|$ increases with flow rate, a negative slope indicates that the frequency loading increases with flow without a corresponding increase in dissipation, whereas a slope near zero suggests that ΔD remains relatively constant. The marginally positive values at $n = 5$ stem from the heightened measurement uncertainty associated with elevated overtones, where the data dispersion amplifies (Figure S5), and should be interpreted cautiously. The results are the gradual decrease in the steepness of the slope from $n = 1$ to $n = 5$, indicating that the area examined at elevated acoustic frequencies yields a greater reactive frequency response in comparison to dissipative loss.

The inter-overtone ratios provide an autonomous assessment of internal consistency. $F1$, $F2$ and $F3$ mean $|\Delta f|$ at $n1$, $n3$, and $n5$ correspondingly, $D1$, $D2$ and $D3$ indicate the ΔD at $n1$, $n3$, and $n5$. Across deionized water and the complete PBS concentration series, the frequency ratios remain comparatively stable: $F2/F1$ is approximately 2.0, $F3/F2$ is approximately 1.25, and $F3/F1$ is approximately 2.5 (Figure 4d–k). This near-conserved scaling indicates that the frequency response varies systematically across the overtone series and is not dominated by random instrumental drift. The dissipation ratios follow a different scaling relationship. $D2/D1$ remains approximately 1.74–1.79, $D3/D2$ remains approximately 0.81–0.87, and $D3/D1$ remains approximately 1.44–1.54. The dissipation ratios therefore do not reproduce the corresponding frequency hierarchy. This mismatch demonstrates that the two QCM-D observables are governed by related but nonidentical components of the interfacial response.

Frequency is primarily associated with the reactive component of the complex acoustic load, including liquid inertia and elastic coupling, whereas dissipation reflects energy lost during each oscillation cycle. The dendritic interface consequently cannot be described adequately as a rigid no-slip surface in contact with a homogeneous Newtonian liquid. Instead, the overtone-dependent ratios identify a mechanically heterogeneous interphase in which surface-bound water, confined liquid, hydrated ions, and bulk liquid contribute differently to frequency loading and energy dissipation. This interpretation is consistent with load-impedance models showing that immersed soft, particulate, and heterogeneous interfacial layers can produce nonlinear and overtone-dependent QCM responses through hydrodynamic coupling.[26–28]

Model-Derived Apparent Slip Is Jointly Programmed by Hydration and Shear

The experimentally measured frequency and dissipation shifts were converted into a normalized apparent-slip parameter using

Downloaded from pubs.acs.org/aamick/article-pdf/18/43/60124/6895925/am-2026-16664d.pdf by DUBLIN CITY UNIV user on 05 November 2026

https://doi.org/10.1021/acsami.6c16664
ACS Appl. Mater. Interfaces 2026, 18, 60124–60136

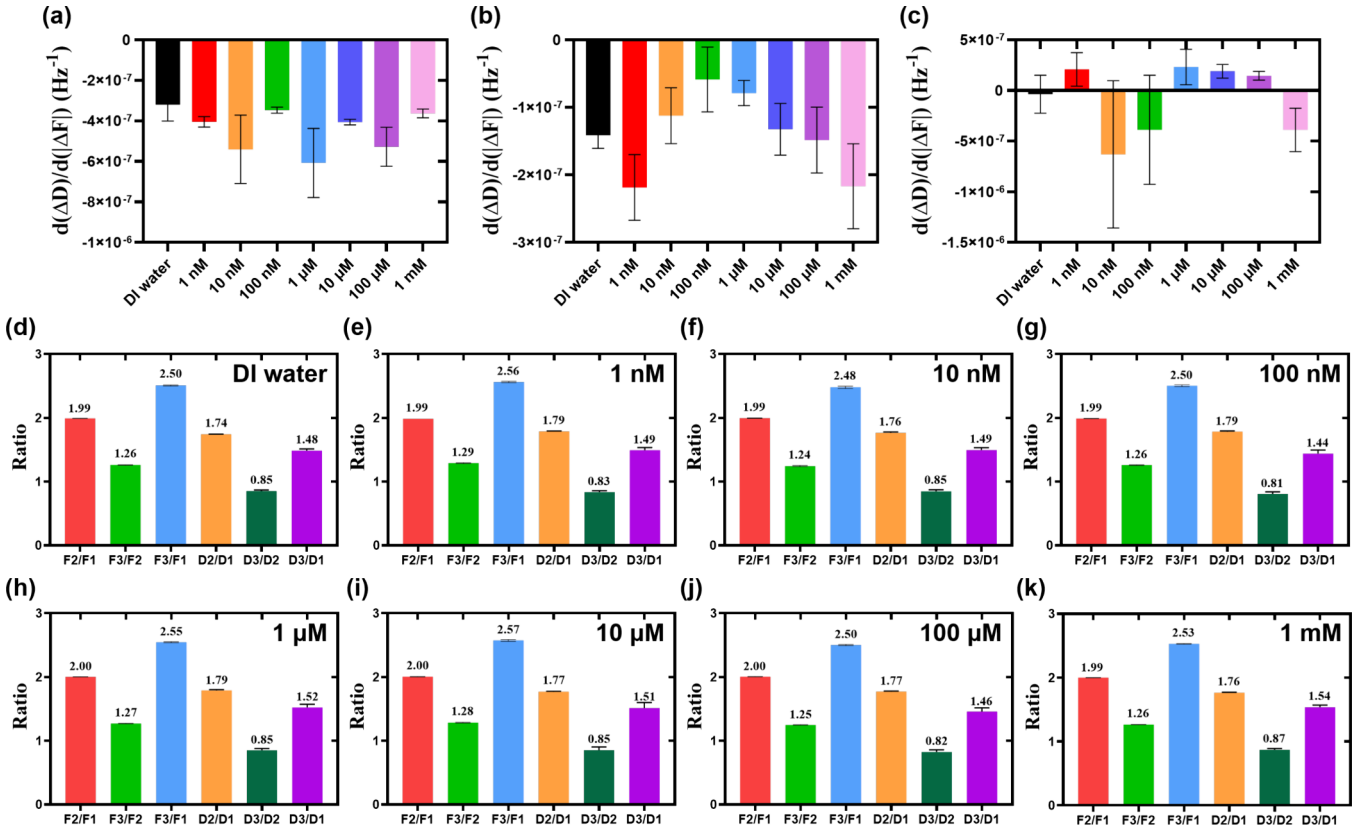


Figure 4. Dissipation–frequency coupling and inter-overtone scaling of the strongly hydrophilic nanostructured solid–liquid interface. (a–c) Slope of ΔD vs $|\Delta f|$, at $n1$, $n3$, and $n5$. The magnitude of slope decreases toward the higher overtones, indicating reduced dissipative loss per unit frequency response in the near-surface region. (d–k) Inter-overtone frequency and dissipation ratios for deionized water and each PBS concentration. The frequency ratios remain comparatively conserved, whereas the dissipation ratios exhibit a distinct scaling hierarchy, indicating that acoustic loading and energy dissipation are not governed by an identical interfacial process.

a dynamic vibrating-interface model. The complex load impedance of the measured interface, Z_L^s, was compared with the corresponding no-slip load impedance, Z_L^{ns}, according to

$$\frac{b}{\delta} = (1+i)\frac{Z_L^s - Z_L^{ns} - i\omega\rho_f l_a}{2\left(Z_L^{ns} + i\omega\rho_f l_a\right)} \quad (3)$$

where b is the model-derived apparent slip length, δ is the acoustic penetration depth, ω is the angular frequency, ρ_f is the liquid density, and l_a is the inertial length assigned to the first interfacial liquid layer. More details on eq 3 can be found in previous works.[37,38] A fixed value of l_a = 0.3 nm was used to represent a molecular-scale first hydration layer. The basis for fixing l_a at this value, along with a sensitivity analysis, is provided in refs.[37,38] Because QCM-D does not directly measure the liquid-velocity profile at the solid boundary, b should not be interpreted as a directly measured velocimetric slip length. Accordingly, the quantity

$$\left|\mathrm{Re}\left(\frac{b}{\delta}\right)\right| \quad (4)$$

is used as a dimensionless descriptor of apparent slip-like interfacial mobility. This terminology is important because the model reports a deviation from the selected no-slip acoustic-load condition rather than direct observation of a Navier velocity profile. The extracted apparent-mobility parameter increases with flow rate at every measured overtone (Figure 5a–c). At $n1$, $|\mathrm{Re}(b/\delta)|$ remains approximately 1.75–1.76 between 1 and 8 mL h^{-1}, increases slightly at 16 mL h^{-1}, and reaches approximately 1.78–1.80 at 32 mL h^{-1} (Figure 5a).

At $n3$, the response increases from approximately 2.98–3.02 at low flow to approximately 3.05–3.11 at 32 mL h^{-1} (Figure 5b). At $n5$, it increases from approximately 3.58–3.70 to approximately 3.75–3.90 over the same flow interval (Figure 5c). We observe two specific features. First, the increase occurs most consistently at the largest flow rates, supporting a flow-activated transition rather than random variation in the acoustic baseline. Second, the magnitude increases with overtone order, indicating that the apparent mobility is strongest in the thinner near-surface region sampled at higher acoustic frequency. These trends parallel the raw QCM-D observations: the largest model-derived apparent mobility occurs under conditions that produce increased frequency loading without a proportional increase in dissipation. The heat maps in Figure 5d–f show that flow rate and ionic strength do not operate independently. Low-flow conditions consistently occupy the lower-mobility region of each map, whereas the largest values are concentrated near 32 mL h^{-1}. Superimposed on this flow dependence is a nonmonotonic ionic-strength dependence. Intermediate and higher PBS concentrations generally increase

Downloaded from pubs.acs.org/aamick/article-pdf/18/43/60124/6895925/am-2026-166644.pdf by DUBLIN CITY UNIV user on 05 November 2026

https://doi.org/10.1021/acsami.6c16664
ACS Appl. Mater. Interfaces 2026, 18, 60124–60136

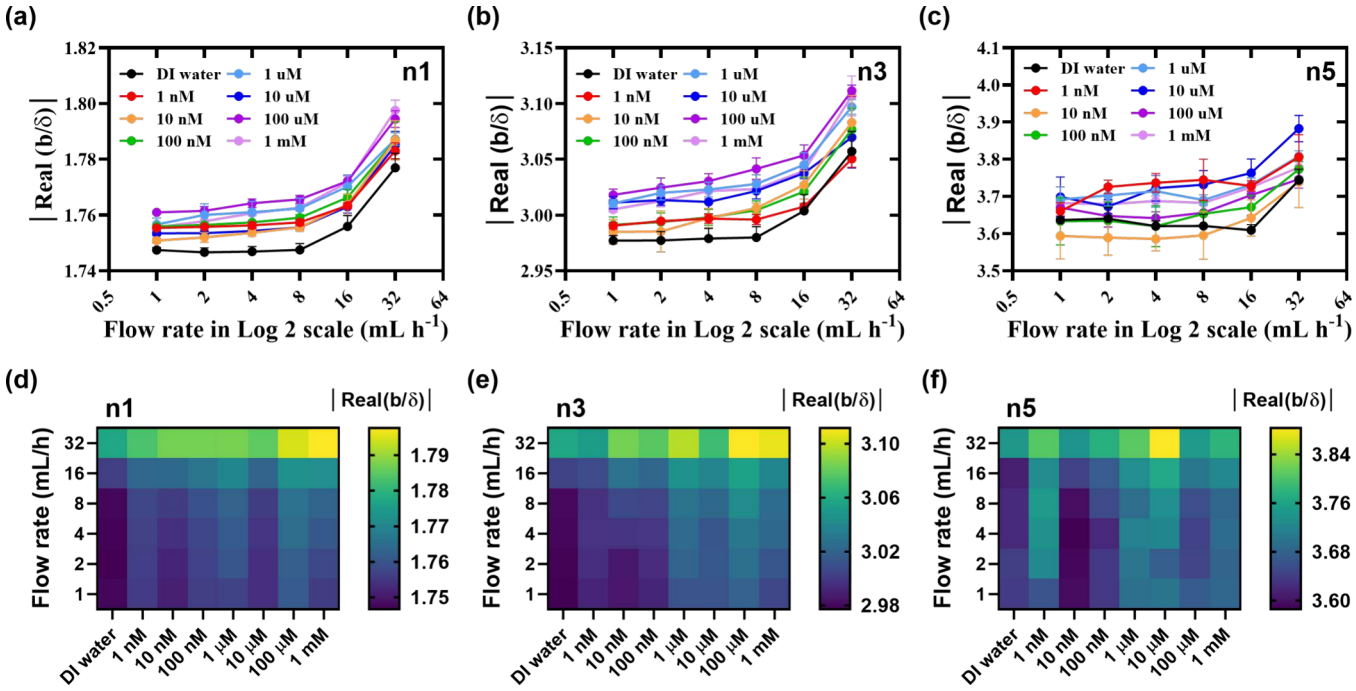


Figure 5. Hydration- and flow-programmed apparent-slip response of the strongly hydrophilic nanostructured solid–liquid interface. (a–c) Real component of the normalized apparent-slip parameter, $|\mathrm{Re}(b/\delta)|$, calculated at $n1$, $n3$, and $n5$ using the dynamic vibrating-interface model with $l_a = 0.3$ nm. The apparent-mobility parameter increases with flow rate and becomes progressively larger at the higher overtones. (d–f) Heat maps of $|\mathrm{Re}(b/\delta)|$ as a function of flow rate and electrolyte concentration. The maps reveal a dynamic interfacial mobility landscape jointly regulated by hydration state and hydrodynamic forcing.

the apparent-mobility parameter relative to deionized water, although the concentration producing the maximum response varies with overtone. This response landscape supports a two-parameter mechanism. Ionic strength defines the molecular state of the EDL-associated hydrated interphase by altering ion–surface association, electrostatic screening, and hydration-shell organization. Hydrodynamic flow then determines the extent to which that pre-existing hydration architecture reorganizes dynamically. The interface is therefore not characterized by a single fixed slip property. Instead, its apparent mobility is programmed by both solution chemistry and hydrodynamic forcing. The model dependence of the absolute values must remain explicit. The calculated magnitude of b/δ depends on the selected no-slip reference, liquid properties, conversion of the QCM-D observables into complex impedance, and the assumed value of l_a. In addition, the flow-dependent values include a contribution from generic flow-cell effects (Figure S8). The central conclusion should therefore be based primarily on the reproducible flow, ionic-strength, and overtone dependences rather than on a single absolute value of the calculated apparent-slip parameter.

Hydrated BSA Interphase Retains Enhanced Apparent Mobility

The biological relevance of the hydration-programmed interface was evaluated by adsorbing bovine serum albumin (BSA) on the dendritic SiO_2 surface and on the bare reference surface under otherwise identical flow conditions (Figure 6). Protein adsorption provides a stringent test of the proposed mechanism because the biomolecular layer increases interfacial complexity, introduces viscoelastic deformation, and carries a substantial quantity of mechanically coupled water.

The frequency shifts measured after BSA exposure are consistently larger on the dendritic surface than on the bare surface. At $n1$, the nanostructured interface produces shifts of approximately 4.6 to 4.8 kHz, compared with approximately 2.5 to 2.6 kHz on the bare surface (Figure 6a). At $n3$, the corresponding values are approximately 8.0 to 8.3 kHz and 5.1 to 5.2 kHz, respectively (Figure 6b). At $n5$, the dendritic surface reaches approximately 11.2 to 11.7 kHz, compared with approximately 7.3 to 7.5 kHz for the bare surface (Figure 6c). These differences should be described as greater protein-associated acoustic loading, rather than as greater dry BSA mass. QCM-D senses the adsorbed protein together with hydrodynamically coupled water, water retained within the protein layer, and liquid trapped by the underlying surface morphology. Combined optical and QCM-D measurements have established that acoustic mass can substantially exceed the nonsolvated molecular mass because of coupled solvent and that surface roughness can further increase the associated-water contribution.[23–25] The enhanced frequency response on the dendritic surface may therefore arise from several coupled contributions, including a larger effective surface area, increased BSA coverage, water retained within the nanostructured morphology, and a more extensively hydrated protein interphase. Without an independent measurement of nonsolvated protein mass, these contributions cannot be uniquely separated. Nevertheless, the data demonstrate that the BSA-associated acoustic interphase formed on the dendritic surface is substantially different from the corresponding layer on the bare electrode.

Downloaded from pubs.acs.org/aamick/article-pdf/18/43/60124/6895925/am-2026-16664d.pdf by DUBLIN CITY UNIV user on 05 November 2026

https://doi.org/10.1021/acsami.6c16664
ACS Appl. Mater. Interfaces 2026, 18, 60124–60136

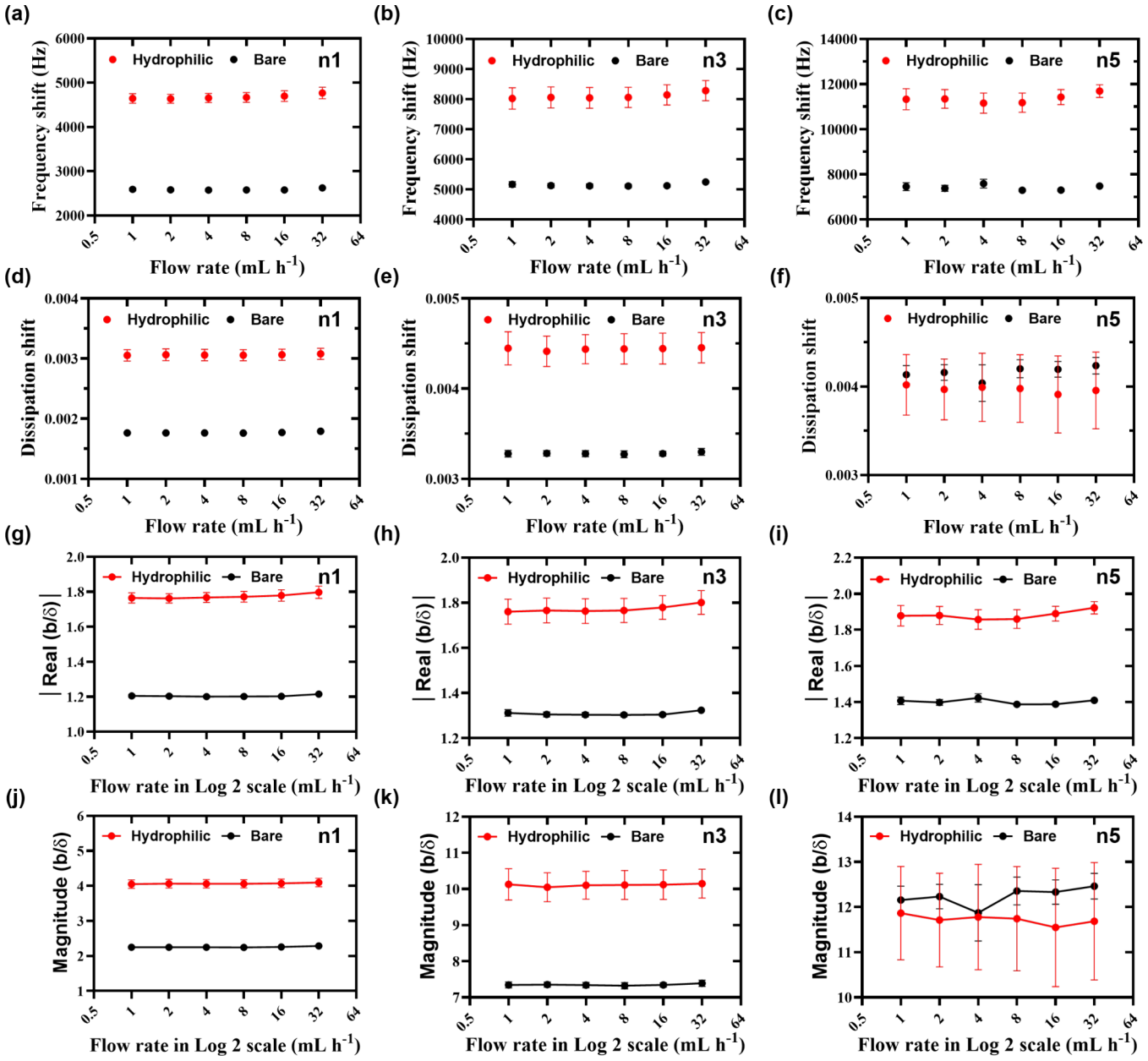


Figure 6. BSA adsorption on strongly hydrophilic nanostructured and bare solid–liquid interfaces. (a–c) Frequency shifts measured after BSA exposure at *n*1, *n*3, and *n*5. The dendritic surface exhibits substantially greater protein-associated acoustic loading than the bare surface. (d–f) Corresponding dissipation shifts. Greater dissipation at *n*1 and *n*3 is consistent with formation of a softer and more hydrated protein interphase on the dendritic surface. (g–i) Real component of the normalized apparent-slip parameter, $|\mathrm{Re}(b/\delta)|$. The dendritic interface retains a larger apparent-mobility response after BSA adsorption at all overtones. (j–l) Magnitude of the normalized response, $|b/\delta|$. The magnitude remains larger on the dendritic surface at *n*1 and *n*3, whereas the *n*5 response exhibits greater uncertainty and partial convergence.

The dissipation response supports this conclusion. At *n*1, ΔD is approximately 3.0×10^{-3} on the dendritic interface and approximately 1.8×10^{-3} on the bare interface (Figure 6d). At *n*3, the corresponding values are approximately 4.4–4.5 $\times 10^{-3}$ and 3.3×10^{-3}, respectively (Figure 6e). The higher dissipation at the lower overtones indicates that the BSA-associated layer formed on the dendritic surface is softer, more hydrated, more viscoelastically heterogeneous, or a combination of these characteristics. At *n*5, the dissipation responses of the two surfaces become more similar, with values of approximately 4.0–4.2 $\times 10^{-3}$ and partially overlapping error bars (Figure 6f). This convergence suggests that the highest overtone weights a thinner region near the silica–protein contact zone, where the mechanical contrast between the interfaces becomes smaller or local heterogeneity produces greater measurement uncertainty. Protein adsorption and interfacial hydration are strongly coupled phenomena. Changes in the organization and mobility of water at a surface can influence both protein attachment and the viscoelastic response measured by QCM-D.[24,25,30]

Despite its greater acoustic loading and higher dissipation, the BSA-modified dendritic surface retains a larger apparent slip-like response than the BSA-modified bare surface (Figure 6g–i).

Downloaded from pubs.acs.org/aamick/article-pdf/18/43/60124/6895925/am-2026-166644.pdf by DUBLIN CITY UNIV user on 05 November 2026

https://doi.org/10.1021/acsami.6c16664
ACS Appl. Mater. Interfaces 2026, 18, 60124–60136

At $n1$, $|\mathrm{Re}(b/\delta)|$ remains approximately 1.76–1.80 on the dendritic surface, compared with approximately 1.20–1.22 on the bare surface. At $n3$, the corresponding values are approximately 1.75–1.80 and 1.30–1.33. At $n5$, the dendritic interface gives approximately 1.86–1.92, whereas the bare interface remains at approximately 1.39–1.42. This observation is mechanistically important because the apparent mobility associated with the dendritic surface is not eliminated by formation of a protein layer. Instead, the nanostructured substrate supports a composite BSA–water interphase that remains more dynamically compliant than the corresponding film on the bare surface. A larger acoustic load therefore does not necessarily imply a more strongly pinned hydrodynamic boundary. The dendritic interface couples more protein-associated material and dissipates more energy, while retaining a larger model-derived real apparent-slip component. The magnitude of the normalized response, $|b/\delta|$, is also larger on the dendritic interface at $n1$ and $n3$ (Figure 6j,k). At $n1$, $|b/\delta|$ is approximately 4.1 on the dendritic surface compared with approximately 2.2–2.3 on the bare surface. At $n3$, the values are approximately 10.0–10.2 and 7.3–7.4, respectively. At $n5$, the magnitude response exhibits greater scatter and partial convergence between the surfaces (Figure 6l). This larger uncertainty indicates that $|b/\delta|$ at the highest overtone is particularly sensitive to local viscoelastic heterogeneity and uncertainty in the complex load impedance. Accordingly, $|\mathrm{Re}(b/\delta)|$, which remains separated between the two surfaces at all measured overtones, provides the more robust comparative descriptor. The weak flow dependence of the BSA frequency, dissipation, and apparent-mobility responses indicates that the adsorbed protein layer remains mechanically stable throughout the tested flow range, as confirmed by the real-time traces in Figure S6. These real-time data reached a stable plateau and showed no systematic change with flow rate. The difference between the dendritic and bare surfaces is therefore unlikely to arise primarily from progressive protein detachment. Rather, it reflects distinct mechanical and hydration states of the protein–solid–liquid interphase.

CONCLUSIONS

This work demonstrates that the dynamic boundary condition of a nanostructured aqueous interface is governed not by wettability alone, but by the coupled effects of surface morphology, hydration, ionic environment, hydrodynamic forcing, and biomolecular adsorption. Dendritic SiO_2 creates a hydroxyl-rich, high-surface area interface that retains strongly associated and geometrically confined water. Contact-angle measurements and DFT calculations support favourable water–surface interactions, while overtone-resolved QCM-D measurements reveal that this hydrated interphase remains mechanically reconfigurable. Electrolyte addition produces a nonmonotonic acoustic response, indicating that intermediate ionic conditions maximize interfacial reorganization rather than simply increasing viscous loading. Under flow, the simultaneous enhancement of $|\Delta f|$ and the model-derived $|\mathrm{Re}(b/\delta)|$, without a proportional rise in dissipation, shows that hydrodynamic forcing drives the hydrated boundary toward a more dynamically mobile state. BSA adsorption modifies this state by forming a hydrated protein-associated layer, yet the dendritic interface retains an enhanced apparent-mobility response.

These findings establish a broader distinction between equilibrium wetting and dynamic interfacial mechanics. Contact angle describes the static wetting state, whereas complex acoustic impedance probes the evolving mechanical coupling among the solid, hydration layer, ions, biomolecules, and adjacent liquid. The term apparent slip is therefore essential because QCM-D measures deviations from a no-slip acoustic model rather than directly resolving the liquid velocity profile. More broadly, the results identify hydration-layer reconfigurability as a design principle for controlling liquid mobility at strongly hydrophilic nanointerfaces. This concept may guide the engineering of biosensors, antifouling coatings, nanofluidic systems, separation membranes, and other technologies in which interfacial hydration and transport are intrinsically coupled.

ASSOCIATED CONTENT

Supporting Information

The Supporting Information is available free of charge at https://pubs.acs.org/doi/10.1021/acsami.6c16664.

SEM characterization of SiO_2 dendrite-coated crystals; concentration- and flow-rate-dependent QCM-D frequency and dissipation responses; overtone-resolved dissipation–frequency trajectories; real-time QCM-D responses during BSA adsorption; and supporting references (PDF)

UV-treated surface (MP4)

Untreated surface (MP4)

AUTHOR INFORMATION

Corresponding Authors

Doojin Lee – *Nanotechnology and Integrated Bioengineering Centre (NIBEC), School of Engineering, Ulster University, 2–24 York Street, Belfast, Northern Ireland BT15 1AP, UK; Department of Polymer Science and Engineering, Chonnam National University, Gwangju 61186, South Korea;* orcid.org/0000-0001-8264-4720; Email: dlee@chonnam.ac.kr

Enda McGlynn – *School of Physical Sciences, Dublin City University, Glasnevin, Dublin 9, Ireland;* orcid.org/0000-0002-3412-9035; Email: enda.mcglynn@dcu.ie

Nikhil Bhalla – *Nanotechnology and Integrated Bioengineering Centre (NIBEC), School of Engineering, Ulster University, 2–24 York Street, Belfast, Northern Ireland BT15 1AP, UK;* orcid.org/0000-0002-4720-3679; Email: n.bhalla@ulster.ac.uk

Authors

Youngho Han – *Nanotechnology and Integrated Bioengineering Centre (NIBEC), School of Engineering, Ulster University, 2–24 York Street, Belfast, Northern Ireland BT15 1AP, UK; Department of Polymer Science and Engineering, Chonnam National University, Gwangju 61186, South Korea*

Aoife Lundberg – *School of Physical Sciences, Dublin City University, Glasnevin, Dublin 9, Ireland*

Jong Sik Kim – *Department of Polymer Science and Engineering, Chonnam National University, Gwangju 61186, South Korea*

Paul Cannon – *Advanced Research Center for Nanolithography (ARCNL), Science Park 106 1098 XG Amsterdam, The Netherlands*

Complete contact information is available at: https://pubs.acs.org/doi/10.1021/acsami.6c16664

Downloaded from pubs.acs.org/aamick/article-pdf/18/43/60124/6895925/am-2026-166644.pdf by DUBLIN CITY UNIV user on 05 November 2026

https://doi.org/10.1021/acsami.6c16664
ACS Appl. Mater. Interfaces 2026, 18, 60124–60136

Author Contributions

[‖]Y.H. and A.L. contributed equally to this paper.

Notes

The authors declare no competing financial interest.

■ ACKNOWLEDGMENTS

This work was partly supported by the Regional Innovation System & Education (RISE) Glocal University 30 Program through the Gwangju RISE Center, funded by the Ministry of Education (MOE) and the Gwangju Metropolitan City, Republic of Korea ((2026-RISE(Glocal University 30)-05-011) and the Korean government (MSIT)(RS-2025-00562401).

■ REFERENCES

(1) Joseph, P.; Tabeling, P. Direct Measurement of the Apparent Slip Length. *Phys. Rev. E* **2005**, *71*, 035303.
(2) Joly, L.; Ybert, C.; Bocquet, L. Probing the Nanohydrodynamics at Liquid–Solid Interfaces Using Thermal Motion. *Phys. Rev. Lett.* **2006**, *96*, 046101.
(3) Honig, C. D. F.; Ducker, W. A. No-Slip Hydrodynamic Boundary Condition for Hydrophilic Particles. *Phys. Rev. Lett.* **2007**, *98*, 028305.
(4) Cottin-Bizonne, C.; Cross, B.; Steinberger, A.; Charlaix, E. Boundary Slip on Smooth Hydrophobic Surfaces: Intrinsic Effects and Possible Artifacts. *Phys. Rev. Lett.* **2005**, *94*, 056102.
(5) Huang, D.; Zhang, T.; Xiong, G.; Xu, L.; Qu, Z.; Lee, E.; Luo, T. Tuning Water Slip Behavior in Nanochannels Using Self-Assembled Monolayers. *ACS Appl. Mater. Interfaces* **2019**, *11*, 32481–32488.
(6) Ishida, H.; Takahashi, K.; Ganesan, V.; Miljkovic, N.; Teshima, H. Hydrophobicity Does Not Affect Water Slip: Insights from Slip Length Mapping. *Nano Lett.* **2026**, *26*, 6698–6704.
(7) Martines, E.; Seunarine, K.; Morgan, H.; Gadegaard, N.; Wilkinson, C. D. W.; Riehle, M. O. Superhydrophobicity and Superhydrophilicity of Regular Nanopatterns. *Nano Lett.* **2005**, *5*, 2097–2103.
(8) Choi, C.-H.; Kim, C.-J. Large Slip of Aqueous Liquid Flow over a Nanoengineered Superhydrophobic Surface. *Phys. Rev. Lett.* **2006**, *96*, 066001.
(9) Holt, J. K.; Park, H. G.; Wang, Y.; Stadermann, M.; Artyukhin, A. B.; Grigoropoulos, C. P.; Noy, A.; Bakajin, O. Fast Mass Transport through Sub-2-Nanometer Carbon Nanotubes. *Science* **2006**, *312*, 1034–1037.
(10) Secchi, E.; Marbach, S.; Niguès, A.; Stein, D.; Siria, A.; Bocquet, L. Massive Radius-Dependent Flow Slippage in Carbon Nanotubes. *Nature* **2016**, *537*, 210–213.
(11) Bakli, C.; Chakraborty, S. Slippery to Sticky Transition of Hydrophobic Nanochannels. *Nano Lett.* **2015**, *15*, 7497–7502.
(12) Israelachvili, J. N.; Pashley, R. M. Molecular Layering of Water at Surfaces and Origin of Repulsive Hydration Forces. *Nature* **1983**, *306*, 249–250.
(13) Raviv, U.; Klein, J. Fluidity of Bound Hydration Layers. *Science* **2002**, *297*, 1540–1543.
(14) Lane, J. M. D.; Chandross, M.; Stevens, M. J.; Grest, G. S. Water in Nanoconfinement between Hydrophilic Self-Assembled Monolayers. *Langmuir* **2008**, *24*, 5209–5212.
(15) Ma, L.; Gaisinskaya-Kipnis, A.; Kampf, N.; Klein, J. Origins of Hydration Lubrication. *Nat. Commun.* **2015**, *6*, 6060.
(16) Donose, B. C.; Vakarelski, I. U.; Higashitani, K. Silica Surfaces Lubrication by Hydrated Cations Adsorption from Electrolyte Solutions. *Langmuir* **2005**, *21*, 1834–1839.
(17) Gaisinskaya-Kipnis, A.; Ma, L.; Kampf, N.; Klein, J. Frictional Dissipation Pathways Mediated by Hydrated Alkali Metal Ions. *Langmuir* **2016**, *32*, 4755–4764.
(18) Schlaich, A.; Kappler, J.; Netz, R. R. Hydration Friction in Nanoconfinement: From Bulk via Interfacial to Dry Friction. *Nano Lett.* **2017**, *17*, 5969–5976.
(19) Han, T.; Cao, W.; Xu, Z.; Adibnia, V.; Olgiati, M.; Valtiner, M.; Ma, L.; Zhang, C.; Ma, M.; Luo, J.; Banquy, X. Hydration Layer Structure Modulates Superlubrication by Trivalent La^{3+} Electrolytes. *Sci. Adv.* **2023**, *9*, eadf3902.
(20) Kanazawa, K. K.; Gordon, J. G. The Oscillation Frequency of a Quartz Resonator in Contact with Liquid. *Anal. Chim. Acta* **1985**, *175*, 99–105.
(21) Rodahl, M.; Höök, F.; Krozer, A.; Brzezinski, P.; Kasemo, B. Quartz Crystal Microbalance Setup for Frequency and Q-Factor Measurements in Gaseous and Liquid Environments. *Rev. Sci. Instrum.* **1995**, *66*, 3924–3930.
(22) Voinova, M. V.; Rodahl, M.; Jonson, M.; Kasemo, B. Viscoelastic Acoustic Response of Layered Polymer Films at Fluid–Solid Interfaces: Continuum Mechanics Approach. *Phys. Scr.* **1999**, *59*, 391–396.
(23) Macakova, L.; Blomberg, E.; Claesson, P. M. Effect of Adsorbed Layer Surface Roughness on the QCM-D Response: Focus on Trapped Water. *Langmuir* **2007**, *23*, 12436–12444.
(24) Bingen, P.; Wang, G.; Steinmetz, N. F.; Rodahl, M.; Richter, R. P. Solvation Effects in the Quartz Crystal Microbalance with Dissipation Monitoring Response to Biomolecular Adsorption: A Phenomenological Approach. *Anal. Chem.* **2008**, *80*, 8880–8890.
(25) Wang, G.; Rodahl, M.; Edvardsson, M.; Svedhem, S.; Ohlsson, G.; Höök, F.; Kasemo, B. A Combined Reflectometry and Quartz Crystal Microbalance with Dissipation Setup for Surface Interaction Studies. *Rev. Sci. Instrum.* **2008**, *79*, 075107.
(26) Johannsmann, D.; Reviakine, I.; Rojas, E.; Gallego, M. Effect of Sample Heterogeneity on the Interpretation of QCM-D Data: Comparison of Combined Quartz Crystal Microbalance/Atomic Force Microscopy Measurements with Finite Element Method Modeling. *Anal. Chem.* **2008**, *80*, 8891–8899.
(27) Meléndez, M.; Vázquez-Quesada, A.; Delgado-Buscalioni, R. Load Impedance of Immersed Layers on the Quartz Crystal Microbalance: A Comparison with Colloidal Suspensions of Spheres. *Langmuir* **2020**, *36*, 9225–9234.
(28) Adamczyk, Z.; Sadowska, M. Hydrodynamic Solvent Coupling Effects in Quartz Crystal Microbalance Measurements of Nanoparticle Deposition Kinetics. *Anal. Chem.* **2020**, *92*, 3896–3903.
(29) Adamczyk, Z.; Sadowska, M.; Żeliszewska, P. Applicability of QCM-D for Quantitative Measurements of Nano- and Microparticle Deposition Kinetics: Theoretical Modeling and Experiments. *Analytical Chemistry* **2020**, *92*, 15087–15095.
(30) Nagasawa, D.; Azuma, T.; Noguchi, H.; Uosaki, K.; Takai, M. Role of Interfacial Water in Protein Adsorption onto Polymer Brushes as Studied by SFG Spectroscopy and QCM. *J. Phys. Chem. C* **2015**, *119*, 17193–17201.
(31) Yang, P.-J.; Hsu, Y.-C.; Li, J.-R.; Luo, S.-C. Quantitatively elucidating the trade-off between zwitterionic antifouling surfaces and bioconjugation performance. *Langmuir* **2024**, *40*, 26259.
(32) Seror, J.; Zhu, L.; Goldberg, R.; Day, A. J.; Klein, J. Supramolecular synergy in the boundary lubrication of synovial joints. *Nat. Commun.* **2015**, *6*, 6497.
(33) Lis, D.; Backus, E. H.; Hunger, J.; Parekh, S. H.; Bonn, M. Liquid flow along a solid surface reversibly alters interfacial chemistry. *Science* **2014**, *344*, 1138–1142.
(34) Cannon, P.; McGlynn, E.; O'Neill, D.; Darcy, C.; Rouse, E.; O'Connor, R.; Freeland, B.; O'Connell, B.; Gaughran, J. Deposition of high-quality, nanoscale SiO_2 films and 3D structures. *Appl. Mater. Today* **2024**, *38*, 102175.
(35) Cannon, P. Metal Oxide Nanostructures for DNA Analysis. Ph.D. thesis; Dublin City University: Dublin, Ireland, **2024**.
(36) Funari, R.; Matsumoto, A.; De Bruyn, J. R.; Shen, A. Q. Rheology of the electric double layer in electrolyte solutions. *Anal. Chem.* **2020**, *92*, 8244–8253.

Downloaded from pubs.acs.org/aamick/article-pdf/18/43/60124/6895925/am-2026-166644.pdf by DUBLIN CITY UNIV user on 05 November 2026

https://doi.org/10.1021/acsami.6c16664
ACS Appl. Mater. Interfaces 2026, 18, 60124–60136

(37) Payam, A. F.; Kim, B.; Lee, D.; Bhalla, N. Unraveling the liquid gliding on vibrating solid liquid interfaces with dynamic nanoslip enactment. *Nat. Commun.* **2022**, *13*, 6608.
(38) Bhalla, N.; Song, Y.; Jo, J.-Y.; Lee, D.; Payam, A. F. Resolving Nanoslip, Solvation Inertia, and Charge Dynamics at Vibrating Solid–Liquid Interface. *Small* **2025**, *21*, 2505067.

Downloaded from pubs.acs.org/aamick/article-pdf/18/43/60124/6895292/5/am-2026-16664d.pdf by DUBLIN CITY UNIV user on 05 November 2026

https://doi.org/10.1021/acsami.6c16664
ACS Appl. Mater. Interfaces 2026, 18, 60124–60136